Optimizing Warm Hydroforming of AA7075 for Enhanced Bipolar Plate Design in Proton Exchange Membrane Fuel Cells

K.T. Anand[1], Dhivakar Poosapadi[2], B.V. Sai Thrinath[3] and V. Vijayan[4]

[1] Department of Mechanical Engineering, Panimalar Polytechnic College, Chennai – 600029, Tamil Nadu, India
[2] Lead Engineer (Mechanical), Quest Global Services North America, 175 Addison Rd, Windsor, CT 06095, USA
[3] Department of Electrical and Electronics Engineering, School of Engineering, Mohan Babu University, Tirupati, Andhra Pradesh 517102, India
[4] Department of Mechanical Engineering, K. Ramakrishnan College of Technology, Samayapuram, Trichy, India - 621 112, India

Corresponding Author Email: ktanandppc@gmail.com

ABSTRACT

The focus of this study is on the development of bipolar plates for proton exchange membrane fuel cells. The warm hydroforming process using an aluminum alloy (AA7075) sheet material was examined. The channel profile (reagent channel width and die upper radius) and bipolar plate geometries (channel layouts-wise) are investigated using finite element (FE) simulations. The chosen aluminum alloy's mechanical and strain behaviors with regard to temperature and strain rate were characterized by initial experiments. The 2D models were created using finite element analysis to define the channel profile. The width of the reagent channel, the die upper radius, and the sheet thickness were all measured using a statistical method. Lastly, the suggested bipolar plate (BP) geometries were tested in 3D using a range of operating temperatures and oil pressures. Finding geometry that might sidestep crucial thinning zones and settings that would work for warm hydroforming were the two main objectives.

1. INTRODUCTION

The environmentally friendly and highly efficient fuel cell (FC) immediately transforms the chemical energy of fuels into electrical energy[1]. With numerous benefits over traditional internal combustion engines, such as (1) a compact design, (2) a high density of power, (3) a low operating temperature, and (4) nearly no harmful emissions, the proton exchange membrane fuel cell (PEMFC) stands out among FC types [2]. The primary parts of a PEMFC are shown in Figure 1. Two of these components are the electrolytic catalyst situated at the boundary of the ion exchange membrane with the supporting layer and the fuel and oxidant conveying BP, also known as the flow plate[3], [4].

The BP is an integral part of the PEMFC, serving both a structural and functional purpose. It is the heaviest part of the device, making it the most important structural component[5]. Mechanically maintaining the stack, delivering fuel and airborne to the conductors, and facilitating current passage over the fuel cell are all crucial activities carried out by the BP. As far as PEMFC stacking configurations go, the so-called plana bipolar configuration is among the best [6] .

To make the proton exchange membrane fuel cell suitable for stationary applications, transportation, and electronics, such as laptops, it may be necessary to improve its efficiency, energy density, or reduce its weight.
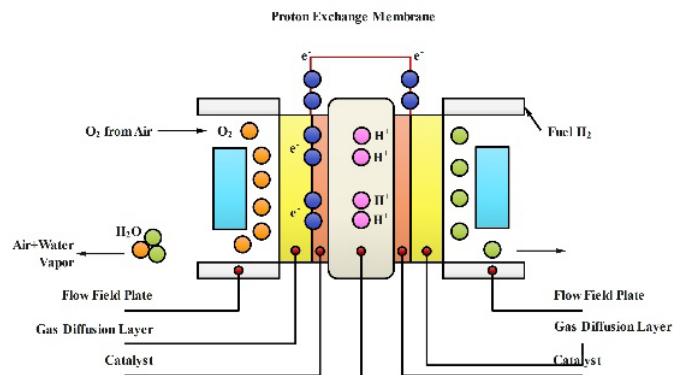

Figure 1. Schematic view of PEMFC

The first solution (efficiency enhancement) was the subject of investigations to determine the optimal operating conditions (pressure and reagent flow rate) for FCs according to certain BPs designs [7]. Reducing the BP's thickness would lead to the second solution, an increase in energy density [8]. Materials that can ensure acceptable mechanical qualities, optimal electrical conductivity, gas impermeability, high corrosion resistance, and low surface electrical resistance are needed to achieve the third solution, which is to reduce weight. Graphite and carbon composites were first utilized to manufacture BPs because of their strong corrosion resistance and low contact

resistance. Carbon composites and graphite do well in FC operating conditions, but they aren't ideal because they're expensive to produce, gas permeable, brittle, and poor electrical and thermal conductors [9]. Because of this, metals are seen as a better option for making BPs.

The effectiveness of sheet metals in BP production has been the subject of multiple investigations. The primary areas of interest have been stain-resistant steel and aluminum alloys. Although stainless steel is easily machined and has excellent mechanical strength, it has low contact resistance, leading to large power losses and a low power density. Researchers[10], [11] investigated the use of hydroforming (HF) as an alternative to the conventional stamping technique to get over these restrictions. They discovered that compared to stamping, the HF technique yields BPs with lower interfacial contact resistance (ICR). Furthermore, the ICR value decreases as the clamping force or maximum oil pressure increases. With an aluminum density of 2.70 g/cm3, aluminum alloys are superior to stainless steel when it comes to meeting the needs of mass reduction[12], [13]. Also, aluminum components can be made using sheet metal methods, which results in a significant improvement in mechanical qualities and a remarkable decrease in thickness, which in turn increases energy density. Typical FC environments have a high corrosion rate for stainless steel and aluminum alloys. In tests examining the effects of ZrN coating on SS316L sheets, corrosion resistance was improved; however, formability and ICR values were reduced [14]. Coated AA5083 specimens had reduced ICR values in experiments compared to uncoated ones, and there was no discernible fluctuation in ICR across different coating thickness values [15].

Using Aluminum alloys to make BPs raises a number of concerns, the most pressing of which is their reduced formability compared to deep drawing steels and the subsequent corrosion risk. Literature confirms, however, that this limitation is circumvented when the procedure is carried out in warm conditions (i.e., at temperatures substantially below 350 °C) and with the appropriate strain rates [16], [17]. In this analysis proposes using Hydro farming at warming criteria (WHF) to manufacture an Aluminum alloy BP. This agrees with earlier research that had demonstrated the practicability of employing the HF method for parts with complicated shapes and more especially, for BP channels [18], [19]. In order to avoid critical thinning zones, this numerical analysis aimed to find the appropriate channel width, die upper radius, BP geometry (the layout of the channels), and channel profiles (the width and radius of the channels). The formed part's qualities were enhanced through the use of 3Dimensional FE simulations to evaluate the process parameters for WHF fabrication of the BP with a modest temperature rise (up to 240 °C). This allowed for the optimization of the manufacturing process without sacrificing complexity or time.

2. INVESTIGATION OF BP GEOMETRIES

This study concentrated on a sheet metal forming process rather than a machining process. Accordingly, the geometries of the bipolar plates (BP) were designed to serve dual purposes: firstly, to enable the creation of channels on both sides of the plate simultaneously, and secondly, to separate the coolant from the reagents. The geometries examined in this research included Spiral (SP), Serpentine (SER), and Multiple Serpentine (MSER), as detailed in Table 1.

Two BPs in a row with the same orientation distinguish BP-type SP cells from BP-type SER and MSER, two PEMFC units that use BPs rotated by 90°. This allows us to merge the forming and connecting operations and simplifies automated cell assembly [20]. The BP-type SP requires the drilling of holes, either after or during the HF process, to provide the reactants, in contrast to the Bipolar plate-type serpentine and multiple serpentine, which can receive cooling water and reactant gases from outside. Efficiently combining the HF process with succeeding procedures, including piercing, can reduce component cycle time and production cost [21], [22].

3. EXPERIMENTAL METHODOLOGY

In this study, the arithmetical analysis were conducted with the BP sheet material AA7075-T6. Therefore, 0.5 mm thick sheets were used in an initial experimental step to describe the mechanical and deformative behavior of the alloy.

3.1 Mechanical characteristics

3.1.1 Instruments

The behavior of the material with respect to temperature and strain rate was assessed by means of tensile testing. Using a laser beam, dog-bone specimens measuring 100 mm in gauge length and 15 mm in breadth were prepared. Unique to this experiment, the apparatus featured nine radiant heaters arrayed around the object. The task of controlling each set of three heaters to attain and sustain the goal temperature (±1%) fell on one arm of the PID controller. Throughout the procedure, a thermocouple was in connection with the sample and provided the data used to create this control. All of the testing was tracked by two 1.3 MP cameras attached to the ARAMIS DIC system. With the images automatically recognized and discretized in a cell grid, displacements and stresses could be continually calculated throughout the procedure without touching the specimen.
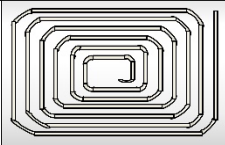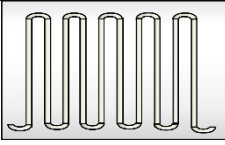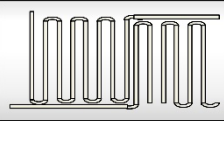
3.1.2 Testing results

Three distinct temperatures RT, 120 and 240, were used in the testing along with two distinct strain rates (SR) of 0.0015 and 0.015 s−1 respectively. For every T and SR level, specimens that were prepared in the direction of rolling were utilized.

Figure 2 shows the curvature of stress flow as a function of actual stress vs strain. The images also show the deformed shape superimposed with maps of the main strain.

Clearly, there is a considerable decrease in flow stress independent of the modest rise in temperature. Figure 2 also shows the SR effect, although it's not as prominent as it is in other Aluminium alloys, such as 7xxx, which are more ductile and show a clearer relationship between temperature and deformative behavior.

Table 1. The geometries that are examined in this study

Geometry	Spiral (SP)	Serpentine (SER)	Multiple Serpentine (MSER)

Higher temperatures (up to 300 °C) may improve performance, mainly in reducing flow stress (although there is a modest change in elongation as well at higher temperatures). Therefore, modest temperature increases (up to 240 °C) were the primary foci of the current investigation.

3.2 Assessing formability

The Nakazima tests were utilized to quantify the maximum strains a material could endure in both main and minor directions under plane stress conditions to assess formability. Forming limit curves (FLC) were determined for each temperature through testing conducted at several temperature levels, similar to tensile tests. Our FLC value was based on ISO 12004-2standard [23], [24].

3.2.1 Equipment

Particularly designed hardware mounted on the tensile testing apparatus was used to conduct the Nakazima tests. A hemispherical punch with a 90 mm diameter, a round draw die with a 110 mm diameter, and a blank holdercircle with a 140 mm radial draw bead were the components. Two 750 W electrical band heaters heated the punch. When the Nakazima punch distorted the blank, the gadget also had two DIC system sensors to gather a detailed strain field.

The specimen's temperature was tracked using a thermocouple attached to the underside and a pyrometer attached to the top surface. The reason it was chosen was because it could withstand temperatures ranging from -25 to +260 °C. A lubricant supplied by Interflon, High Temperature Grease contains additives, synthetic oil, inorganic thickener, and Teflon®. In addition, a 20 kN blank holding force was employed to prevent material drawing. The specimens were characterized geometrically by having a constant length but different widths, as per the guidelines of the ISO 12004-2 standard.

A full FLC description should include at least five geometries. For the Nakazima test, only four geometries were utilized: 30, 80, 130, and 180 mm in width, due to the high cost of conducting experiments in heated circumstances. The FLCs were assessed using supplementary data obtained from the tensile test.

3.2.2 Testing results

Temperatures of 120°C, 240°C, and room temperature were used for the experiments. Throughout all testing, the punching speed remained constant at 30 mm.min^{-1}. Meanwhile the sample was heated by the punch during the test, its temperature had to be checked continuously to make sure it fractured at the exact temperature. The experimental design included a variety of specimen types, as indicate in Table 2. The use of warped sheets served to emphasize how strain levels were affected by rising temperatures. This investigation followed the process for evaluating FLCs as laid out in the ISO Standard. Examining the distribution of strain over specific cross sections is the first step. Bending the residual strain distribution on each side of the neck can restore the strain distribution right before necking begins after the strain spots in the necked area are gone. In order to evaluate the limit strains that FLCs are capable of withstanding, the following procedures were followed: Creating the essential parts, such as the neck (three pieces that span the crack line, 20 mm in length on either side of the crack, with a minimum of 10 points each). Depending on the strain measured at the locations corresponding to the inner boundaries of Br and Bl, one needs to identify the outside boundaries and the ideal fit window width in order to produce the optimal curve approximation for both sides of the neck. It is required to assess the best-fit inverse parabola ($f1(x)=1/(ax2+ bx +c)$) in order to ascertain the required upper limit for the major strain ($\varepsilon1$), which can incorporate strain data in both the side windows. In a roundabout way, we can determine the upper limit for the minor strain ($\varepsilon2$) by comparing it to the genuine thickness strain, which we can get by solving for $\varepsilon3=-\varepsilon1-\varepsilon2$. Extra data points were extracted from the tensile tests by taking into account the crucial strain $\varepsilon1 - \varepsilon2$ before to the occurrence of necking, which is defined as the departure of the strain path from linearity. Separate equations were used to fit the left and right side points, however the same intercept was set with the $\varepsilon1$ axis (FLD0) because according to the ISO standard, "in-house" functions can be used for the regression of $\varepsilon1- \varepsilon2$ data. A linear equation was utilized for data with ή2<0, and a second-order polynomial equation for data with $\varepsilon2>0$. Our data fitting strategy yielded FLCs with a Hill-Swift shape, which is superior to authors [25] use of experimental data from biaxial forming tests to solve a single second-order polynomial equation.

Using the tensile test specimen and four different specimen geometries, Fig 4 displays the Forming limit curves at three different heat levels.

The FLC at RT agrees well with the experimental results [26], [27]. Furthermore, at temperatures above room temperature, AA7075 shows an improvement in formability that is almost never reported in literature. Although there is a large discrepancy in the strain values, this result is consistent with the data about the degree of variance. Experimental data points surrounding a broken area on rectangular cup components are used to establish the ideal fitting producing limit band in the aforementioned research. Even though it appears less limit than other aluminium alloys, the studied alloy improves in terms of formability when considering the imposed
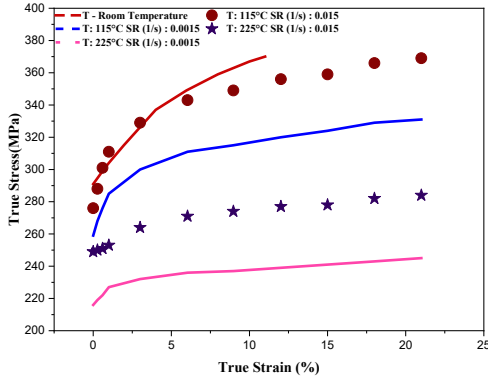
(albeit relatively limited) temperature increase.

Figure 2. Evaluation of true stress of the AA7075 at various strain rate and temperature levels
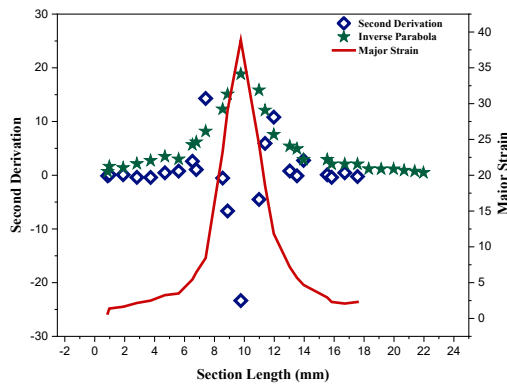

Figure 3. An illustration of the outcomes achieved by utilizing the ISO standard approach for the assessment of range strains
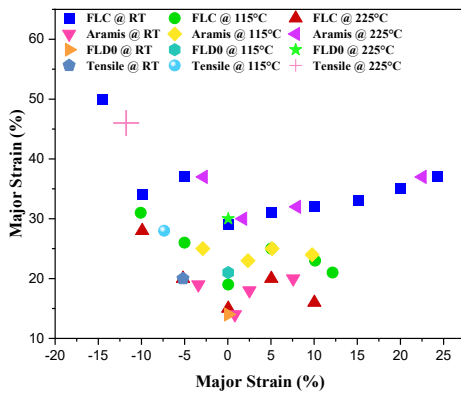

Figure 4. Process of creating limit curves at various temperatures

4. 2D MODEL-BASED CHANNEL PROFILE ANALYSIS

The goal of conducting this low-time 2D analysis was to examine how different channel geometry factors affected the formation process.

4.1 Description of 2-Dimensional FE model

Since the only purpose of the simulations was to study the impact of geometrical characteristics, we assumed RT and a maximum forming pressure of 450 bar. Use of ABAQUS\Standard was employed to generate the 2D planar strain model for the HF procedure. A rigid surface model of the die was used to create the blank's mesh, and a typology of four elements along the thickness called plane strain (PE) quadrilateral elements was selected. We used flow stress data at room temperature to predict the material's behavior. Although numerous alternative appropriate functions for aluminium alloy modeling exist [28], the Von Mises yield function was chosen for the yield surface in this investigation. Indeed, more intricate testing, particularly at high temperatures is necessary for the adoption of better yield criteria that can simulate the "anomalous" behavior of aluminium alloys [29]. Others that modelled the plastic behavior of aluminium alloys verified the use of the Von Mises yield behavior and found a small but respectable discrepancy in their findings [30], [31].

4.2 Analyze variables and circumstances

This study used a design-of-experiment technique to identify the most influential geometrical features of the channel profile on the formation process. According to the available literature, the following are the most important characteristics of an FC BP channel's design: R is the upper die radius, h is the channel depth, F is the width of fuel channel, and S is the width of the rib that are next to each other. A design variable called sheet thickness (t) affects the portion of the channel that chemicals and cooling water go through. Make the number of design variables equivalent to the radius of the die (R= h) by setting the channel depth to equal to one. According to authors[32], [33] finds that the optimal values for the channel depth and transition radius are identical, taking into account both the formability and response performance. Since the present study found that the rib width did not affect the formation process, it was not considered.

To examine the interplay between width of reagent channel (F), Radius of upper die (R), and thickness of sheet (t), three parameters were simultaneously investigated using a full factorial design (FFD) by changing the amounts of the components. Table 3 details all of the FE simulations.

A response measurement's individual circumstances are indicated by each combination of factor levels. As a response parameter, the analysis specifically made use of the following objective function.

$$Obj = \ln\left(\frac{h_{eq}}{t_{eq}}\right) \quad (1)$$

The teq is the ratio of the sheet's initial thickness to the produced blank's minimum thickness. The heq is the ratio of the die's depth to the produced sheet's height. The two parameters are calculated when the highest-pressure hits 450 bar, which is the end of the forming process.

Table 2. Full Factorial Design of FE simulations

S. No	*Radius (R)*(mm)	*Width (F)*(mm)	*Thickness (t)*(mm)

1	0.9	2.5	0.3
2	0.6	1.5	0.4
3	1.2	1.5	0.4
4	0.3	3.5	0.4
5	1.2	3.5	0.4
6	0.9	0.5	0.6
7	0.3	2.5	0.6
8	1.5	2.5	0.6
9	0.9	2.5	0.6
10	0.9	3.5	0.6
11	0.6	1.5	0.8
12	1.2	1.5	0.8
13	0.6	3.5	0.8
14	1.2	3.5	0.8
15	0.9	2.5	1.0

4.3 Investigation of 2- Dimensional Finite element Results

A numericalanalysis was employed to analyze the data through the 2-level Full factorial design. The components' statistical significance was evaluated using the analysis of variance technique. With an R^2 of 98.12%, the regression model that used simulation data to extrapolate showed that it was very well at fitting the input data. Each effect (linear and interaction) has a corresponding probability value (p value) and its corresponding percentage weight (Table 4).

The p-value indicates the likelihood of making an error when assessing the impact of a factor on the variation of the mean value. It helps determine which factors affect the response parameter in Equation 1. All main effect terms have p values below the chosen confidence level of 0.05. There are substantial interactions between the other two components, and factor F shows a non-linear impact.

A Response Surface figure in Fig. 5 summarizes simulation findings, with the third parameter (R) set at a fixed intermediate value of 0.8 mm.

Table 3 Regression model coefficients' weights and corresponding p-values for relevant factors influencing BP channel shape

Term	Coefficient	*p* value
Constant	2.6715	0.000
Radius (R) (mm)	-0.2599	0.011
Width (F) (mm)	-0.6449	0.000
Thickness (t) (mm)	-2.6549	0.000
Radius (R) (mm)*Radius (R) (mm)	0.429	0.008

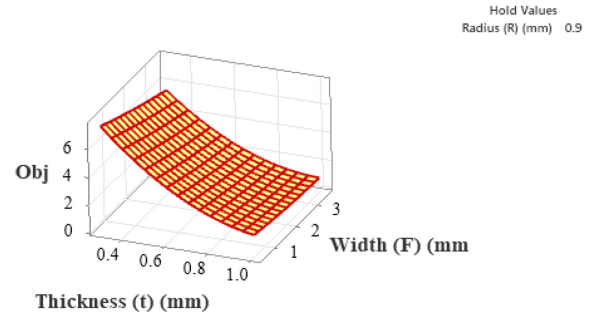|		
Width (F) (mm)*Width (F) (mm)	0.0940	0.305
Thickness (t) (mm)*Thickness (t) (mm)	1.078	0.000
Radius (R) (mm)*Width (F) (mm)	0.135	0.251
Radius (R) (mm)*Thickness (t) (mm)	-0.070	0.590
Width (F) (mm)*Thickness (t) (mm)	0.3805	0.012

Figure 5. 2D surface plot of Obj, F and t at R=0.9mm

Minimizing the function Obj by lowering the sheet thickness to the greatest extent possible is crucial for optimizing the aluminium alloy's behavior. The outcome was the selection of t=0.5 mm as the value to be used for subsequent analysis. Figure 6's contour plot illustrates the connection between the response parameter values and the two parameters that influence them, F and R. As can be seen from the graph, increasing parameter F is necessary for minimizing the objective function. The function Obj will return values in the lowest-value region regardless of the value of R if the value is greater than 2.5 mm. The sheet is made with minimal thickness reduction to attain the optimum depth. We chose the 3.5 mm wide channel profile with a relatively high 1.2 mm roughness value for the 3D numerical simulations that will be detailed in the next section.

According to the authors [34], [35], the ideal channel depth for fuel optimization is 1.5 mm. In addition, applying the methodology suggested in the preceding study, the current analysis found that the value of F would indicate an approximate 80% hydrogen consumption, not a maximum. The results of this investigation align with Peng et al.'s findings, indicating that a die upper radius of around 1.5 mm is optimal for maximizing formability and reducing the danger of fracture owing to material thinning.
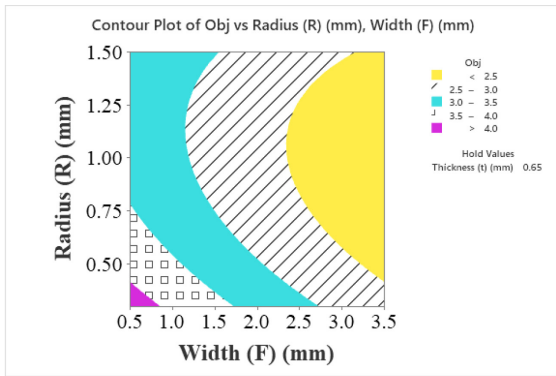
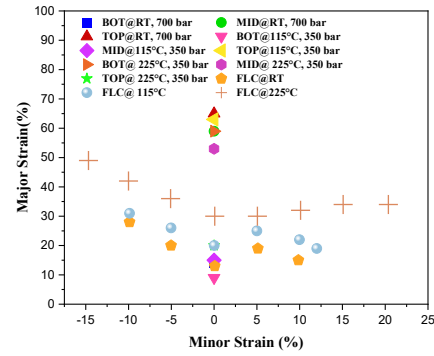**Figure 6**. 3 D plot of width and Radius with respect to Obj

Figure 7. Conditions of strain at numerous profile points along the Bipolar plates Spiral at varying temperatures and pressures

5. INVESTIGATION OF BPHFBY 3DMODELS

The 3D models were used to analyze the WHF method for manufacturing the three various forms of BP. Die shape, which differed between BP geometries, and process parameters including temperature and pressure were both investigated in the investigations.

5.1 Specification of3- Dimensional FE model

To analyze the WHF process parameters and various BP geometries, the commercial finite element package ABAQUS/Explicit (v. 6.10) was utilized. In contrast to the rigid geometries, the sheet was considered a malleable part of the design. Between the sheet and tool surfaces, a friction coefficient of 0.05 was found. That small figure is reasonable considering the oil that is present between the blank, the blankholder, and the die. Since lubricants made of mineral oil have a much lower viscosity at higher temperatures, confirmation should be done at temperatures above room temperature. This two-dimensional model was fitted with the Von Mises yield function. Research into the hardening process of the chosen Aluminium alloy led to the use of a linear pressure profile in simulating that process.

5.2 Study o f3- Dimensional FE results

Room temperature (RT), 120°C, and 240°C were the same temperatures used in the experimental study and in the numerical simulations. The WHF process required a pressure of 350 bar at working temperature, whereas the HF process required 700 bar at room temperature. These two amounts of pressure were defined according to the working temperature. Constraints in the experimental equipment designed for future trials caused the pressure level disparity. The system consists of an electro-hydraulic press machine with a 500 kN capacity and a heated die that can reach 350 °C. Additionally, there is an oil pressurizing unit that can run at 350 bar with hot oil and up to 750 bar at ambient temperature.

Experimental Forming Limit Diagrams of the examined aluminium alloy were contrasted with the outcomes of the finite element simulation. To better gauge the frequency of critical strain conditions, we compared the strain pairings at key sites with the FLC.

In order to determine which part of the channel profile to study, we compared the changes in major and minor strains at three locations: the BOT, TOP, and MID sections of the channel, as illustrated in Figure 7's scheme. This analysis utilized the BP geometry SP.
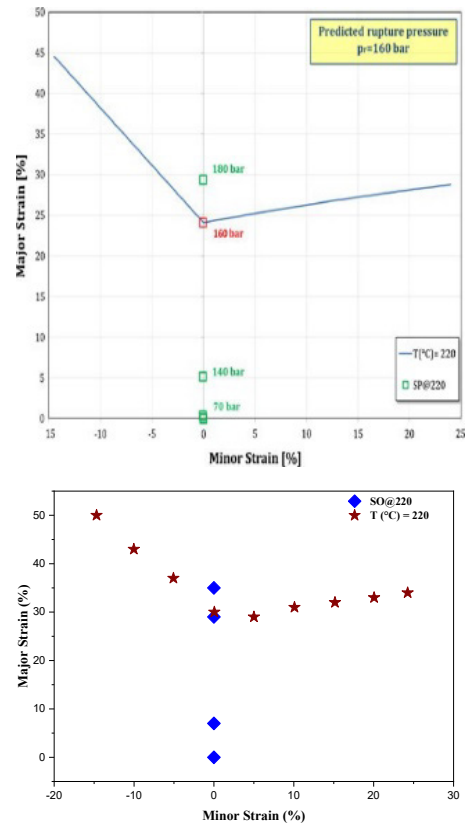

Figure 8. Maximum pressure level numerical evaluation with spiral at 240 °C

For every temperature and maximum pressure, Figure 7 shows the fracture localization diagram (FLD) of the tested aluminium alloy versus strain circumstances (major and minor strain pairings). The duration that the middle of the inlet points laterally the shape of the bipolar plates type being considered are unsupported during formation is a significant issue. This paved the way for its use in later studies. Results from the 240

°C test, as well as the SP die shape used to determine the maximum pressure level, are shown in Figure 8. For this assessment, we compared the strain path—a representation of the process's evolution of major and minor strains—of the most important area in the middle of the inlet (MID) with the FLC that matched the operating temperature.

Table 4. Results summarized from simulations of all three BP types with varying pressure and temperature settings

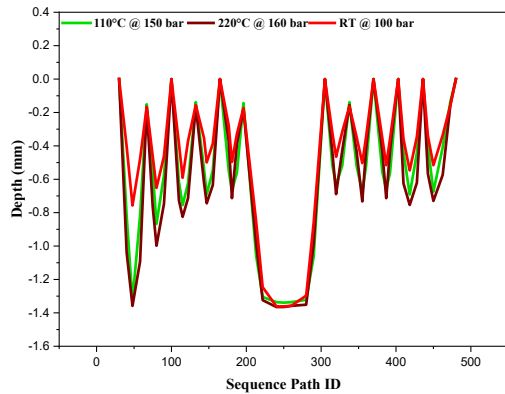| Geometry	Spiral	Serpentine	Multiple Serpentine
Maximump(bar)	100	70	30
Temperature(°C)	RT	240	RT
MaximumPEEQ	23%	24%	20%
Maximump(bar)	150	30	50
Temperature(°C)	120	RT	120
MaximumPEEQ	23%	8%	25%
Maximump(bar)	160	40	80
Temperature(°C)	240	120	240
MaximumPEEQ	30%	19%	28%

Figure 9. The SP geometry's channel profiles taken at various temperatures

Table 4 summarizes the results of all the simulations using the BP geometries indicated earlier. Stress plot, PEEQ, and pressure level at maximum were used for this purpose. Comparisons of table 4 illustrate that primarily how BP geometry affects the process, especially with respect to limit pressure. It is obvious that the Bipolar plates geometricalspiral displays the maximum pressure limit range (beyond which break is anticipated) regardless of the temperature. Using the lowest pressure levels is made possible by the Bipolar plates geometricalserpentine, which appears to be the maximum significant while operating in hot settings (120 or 240 °C). Working in warm environments consistently produces the highest levels of pressure. Limit pressures are higher than RT pressures for all geometries due to the fact that under these conditions, formability increases while material strength decreases only little.

Unlike the SER and MSER BP geometries, the PEEQ maps for BP geometry SP simulations do not reveal detrimental strain localizations when it comes to strain distributions.. Notably, the PEEQ follows a similar (rising) trend as a function of temperature for all three geometries. Even though the maximum PEEQ values in the SER and MSER BP geometries are comparable, there are very few locations where the strain develops and ruptures at low working pressure rather quickly.

Table 4 shows that parameter T, which controls the strain-rise and limit pressure levels, is crucial to the process. Examining the channel profiles across the whole BP following manufacturing is intriguing due to the area-specific data supplied by the greatest PEEQ strain level. With the given limit pressure settings, the channel profiles are shown in Figure 9. Here we look at the BP geometry SP in particular, which shows the maximum PEEQ with increasing temperature.

As a result of the significant improvement, it is clear that the profiles under heated conditions closely resemble the die cavity's shape. The fact that there are only minimal differences when comparing the channel profiles at 120 °C and 240 °C is more noteworthy, though. There is mounting evidence from this discovery that the benefits of a warmer planet are diminishing. By increasing the forming pressure from 10 to 20bar at 200 °C, they found that the same alloy exhibited a die filling increase of 60 to 83% in their HF tests.. Though the identical forming pressure improved die filling at 300 °C, it was barely noticeable.

Considering the difficulties in getting 240 °C (via oil and die) and the improvement in die cavity filling, it seems that adopting a temperature level higher than 120 °C is uncomfortable.

6. CONCLUSIONS

This study looked at three different BP geometries: SER, SP, and MSER. The geometries of the HF-and thin-sheet-lightweight-assumed-AA7075 made BPs were designed with two limitations in mind. To begin, the forming stage could not have proceeded without the canals on either side of the BP simultaneously taking shape. Second, coolant and reagents have to be able to be separated by the channel arrangement. Since these geometries can drastically cut component thickness, which in turn increases the PEMFC's specific energy output and/or decreases the cell's weight, they are all good options for use in industrial settings. As an illustration, the suggested Bipolar platessort can be added to proton exchange membrane fuel cell stacks and utilized as a power source for small electric vehicles because of their larger than minimal active area.

A key finding from early experiments with the AA7075 alloy is that its strength and formability are both influenced by temperature. The 2D and 3D finite element models were used in the numerical analysis, which enabled:

- A description of the ideal BP channel form within the parameters investigated (Radius=0.5 mm, Width=3.5 mm).
- The forming process was studied with respect to different BP geometries; one of them, the SP geometry, had a uniform strain distribution and allowed the maximum forming pressure value to be adopted independently of working temperature.
- Focusing on the fact that the outline at 240 °C was most

comparable to the die cavity profile (using SP geometry), an examination of the huge impact of temperature on the hydroforming of a Bipolar plates is presented, with the caveat that a moderate rise of up to 120 °C could offer the best process improvement.

In the future, this research will focus on the following goals: (1) Looking into the effects of anisotropy on material characteristics; (2) Determining how well a suitable yield criterion models the anisotropy in finite element simulations of the warming hydrofarming process; (3) Utilising the Warming hydro- and Superplastic Forming pressing tool for testing purposes; and (4) validating numerical results and assumptions.

REFERENCES

[1]   E. Dur, O. N. Cora, and M. Ko, 2011, "Experimental investigations on the corrosion resistance characteristics of coated metallic bipolar plates for PEMFC," Int J Hydrogen Energy, vol. 36, no. 12, pp. 7162–7173. DOI: 10.1016/j.ijhydene.2011.03.014

[2]   G. Palumbo and Antonio Piccininni, 2013, "Numerical–experimental investigations on the manufacturing of an aluminium bipolar plate for proton exchange membrane fuel cells by warm hydroforming. The International Journal of Advanced Manufacturing Technology 69. PP. 1-4. DOI: 10.1007/s00170-013-5047-1

[3]   H. T. Ghadikolaee, M. Elyasi, F. A. Khatir, and M. Hosseinzadeh, 2017, "Experimental investigation of Fracture in rubber pad forming of bipolar plate's micro channels," in Procedia Engineering, pp. 1647–1652. DOI:10.1016/j.proeng.2017.10.1093

[4]   O. A. Alo, I. O. Otunniyi, and H. Pienaar, 2019, "Manufacturing methods for metallic bipolar plates for polymer electrolyte membrane fuel cell," Materials and Manufacturing Processes, vol. 34, no. 8, pp. 927–955. DOI:10.1080/10426914.2019.1605170

[5]   Thiyagarajan, K., Jayaraman, M., Vijayan, V., Ramkumar, R. (2020). Cluster analysis of lost foam casted Al-Zn-Mg-Cu alloy with K–Mean algorithm. Journal of New Materials for Electrochemical Systems, Vol. 23, No. 1, pp. 45-51. DOI:10.14447/jnmes.v23i1.a09

[6]   M. Wu, C. Lu, and Y. Su, 2011, "Forming numerical simulation of proton exchange membrane fuel cell metallic bipolar plates," in Proceedings - 2012 3rd International Conference on Digital Manufacturing and Automation, ICDMA 2012, pp. 426–429. DOI: 10.1109/ICDMA.2012.102

[7]   H. Janßen, A. Edelmann, T. Mildebrath, P. Müller, W. Lehnert, and D. Stolten, 2018, "Design and experimental validation of an HT-PEFC stack with metallic BPP," Int J Hydrogen Energy, vol. 43, no. 39, pp. 18488–18497. DOI:10.1016/j.ijhydene.2018.08.058

[8]   Roseline, S., Paramasivam, V., Parameswaran, P., Antony, A.G. (2019). Evaluation of mechanical properties and stability of Al 6061 with addition of ZrO2 And Al2O3. Journal of New Materials for Electrochemical Systems, Vol. 22, No. 1, pp. 21-23. DOI:10.14447/jnmes.v22i1.a05

[9]   R. Girimurugan, C. Shilaja, S. Mayakannan, S. Rajesh, and B. Aravinth, 2022, "Experimental investigations on flexural and compressive properties of epoxy resin matrix sugarcane fiber and tamarind seed powder reinforced bio-composites," in Materials Today: Proceedings, pp. 822–828. DOI:10.1016/j.matpr.2022.04.386

[10] Loganathan, M., Dinesh, S., Vijayan, V., Karuppusamy, T., Rajkumar, S. (2020). Investigation of mechanical behaviour on composites of Al6063 alloy with silicon, graphite and fly ash. Journal of New Materials for Electrochemical Systems, Vol. 23, No. 1, pp. 36-39. DOI:10.14447/jnmes.v23i1.a07

[11] S. Mustefa Beyan, S. Venkatesa Prabhu, T. K. Mumecha, and M. T. Gemeda, 2021, "Production of alkaline proteases using Aspergillus sp. isolated from injera: RSM-GA based process optimization and enzyme kinetics aspect," Curr Microbiol, vol. 78, pp. 1823–1834. DOI:10.1007/s00284-021-02446-4

[12] T. Bothiraj, K. Boopathi, K. Kalaiselvan, A. Benham, and S. Mayakannan, 2022, "Experimental investigations on mechanical and wear behavior of waste marble dust and coconut fiber reinforced hybrid bio composites," in Materials Today: Proceedings, pp. 2239–2242. DOI:10.1016/j.matpr.2022.08.441

[13] S. Mayakannan, R. Rathinam, Rajasekaran Saminathan, R. Deepalakshmi, Mahesh Gopal, J. Justin Maria Hillary, S. Nanthakumar, V. Y. Ganvir, Pallavi Singh, 2022, "Analysis of Spectroscopic, Morphological Characterization and Interaction of Dye Molecules for the Surface Modification of TiB2 Nanoparticles", Journal of Nanomaterials, vol. 2022, Article ID 1033216, 9 pages. DOI:10.1155/2022/1033216

[14] E. Dur, O. N. Cora, and M. Ko, 2011, "Effect of manufacturing conditions on the corrosion resistance behavior of metallic bipolar plates in proton exchange membrane fuel cells," J Power Sources, vol. 196, no. 3, pp. 1235–1241. DOI:10.1016/j.jpowsour.2010.08.052

[15] D. Dinesh Kumar, A. Balamurugan, K. C. Suresh, R. Suresh Kumar, N. Jayanthi, T. Ramakrishnan, S. K. Hasane Ahammad, S. Mayakannan, S. Venkatesa Prabhu, 2023, "Study of Microstructure and Wear Resistance of AA5052/B4C Nanocomposites as a Function of Volume Fraction Reinforcement to Particle Size Ratio by ANN," J Chem, vol. 2023. DOI:10.1155/2023/2554098

[16] R. Ramesh, H. Palanivel, S. Venkatesa Prabhu, B. Z. Tizazu, and A. A. Woldesemayat, 2021, "Process development for edible film preparation using avocado seed starch: response surface modeling and analysis for water-vapor permeability," Advances in Materials Science and Engineering, vol. 2021, pp. 1–7. DOI:10.1155/2021/7859658

[17] B. Tessema, G. Gonfa, S. M. Hailegiorgis, S. V. Prabhu, and S. Manivannan, 2023, "Synthesis and characterization of silver nanoparticles using reducing agents of bitter leaf (Vernonia amygdalina) extract and tri-sodium citrate," Nano-Structures & Nano-Objects, vol. 35, p. 100983. DOI:10.1016/j.nanoso.2023.100983

[18] C. Turan, O. N. Cora, and M. Koç, 2011, "Effect of manufacturing processes on contact resistance

characteristics of metallic bipolar plates in PEM fuel cells," Int J Hydrogen Energy, vol. 36, no. 19, pp. 12370–12380. DOI:10.1016/j.ijhydene.2011.06.091

[19] J. Zhang, R. Wang, and Y. Zeng, 2022, "Hydroforming rules and quality control parameters analysis for metal bipolar plate," Eng Fail Anal, vol. 132. DOI:10.1016/j.engfailanal.2021.105919

[20] I. S. N. V. R. Prasanth, Prabahar Jeevanandam, P. Selvaraju, K. Sathish, S. K. Hasane Ahammad, P. Sujatha, M. Kaarthik, S. Mayakannan, Bashyam Sasikumar, 2023, "Study of Friction and Wear Behavior of Graphene-Reinforced AA7075 Nanocomposites by Machine Learning," J Nanomater, vol. 2023. DOI:10.1155/2023/5723730

[21] Palanivel Hemalatha, Ebrahim M. Abda, Shipra Shah, S. Venkatesa Prabhu, M. Jayakumar, N. Karmegam, Woong Kim, M. Govarthanan, 2023, "Multi-faceted CRISPR-Cas9 strategy to reduce plant based food loss and waste for sustainable bio-economy–a review," J Environ Manage, vol. 332, p. 117382. DOI:10.1016/j.jenvman.2023.117382

[22] R. Srinivasan, R. Deepalakshmi, J. Baskaran, N. Ashok, S. V. Prabhu, and T. Pradeep, 2023, "Investigation on the mechanical properties of micro-sized B4C particles reinforced with FSW of aluminium alloy composites," Mater Today Proc. DOI:10.1016/j.matpr.2023.05.476

[23] C. Turan, Ö. N. Cora, and M. Koç, 2012, "Contact resistance characteristics of coated metallic bipolar plates for PEM fuel cells - Investigations on the effect of manufacturing," Int J Hydrogen Energy, vol. 37, no. 23, pp. 18187–18204. DOI:10.1016/j.ijhydene.2012.09.042

[24] S. Chauhan, V. Senthilkumaran, H. More, and S. Arikapudi, "Characterization Methodology Development for PEM Fuel Cell Bipolar Plate," in 2021 IEEE Transportation Electrification Conference, ITEC-India 2021. DOI:10.1109/ITEC-India53713.2021.9932517

[25] B. Ramesh, S. Sathish Kumar, A. H. Elsheikh, S. Mayakannan, K. Sivakumar, and S. Duraithilagar, "Optimization and experimental analysis of drilling process parameters in radial drilling machine for glass fiber/nano granite particle reinforced epoxy composites," in Materials Today: Proceedings, 2022, pp. 835–840. DOI:10.1016/j.matpr.2022.04.042

[26] F. G. Boyacı San and O. Okur, 2017, "The effect of compression molding parameters on the electrical and physical properties of polymer composite bipolar plates," Int J Hydrogen Energy, vol. 42, no. 36, pp. 23054–23069. DOI:10.1016/j.ijhydene.2017.07.175

[27] F. G. Boyaci San, I. Isik-Gulsac, and O. Okur, 2013, "Analysis of the polymer composite bipolar plate properties on the performance of PEMFC (polymer electrolyte membrane fuel cells) by RSM (response surface methodology)," Energy, vol. 55, pp. 1067–1075. DOI:10.1016/j.energy.2013.03.076

[28] A. Olayinka and W. J. Emblom, 2022, "Surface roughness of AISI 1010 and AISI 304 of PEMFC bipolar plates with microscale hydroformed capillary channels," Proc Inst Mech Eng B J Eng Manuf, vol. 236, no. 10, pp. 1332–1340. DOI:10.1177/09544054221077772

[29] A. Olayinka and W. J. Emblom, 2021 "Numerical investigation of bipolar plates manufactured using hydroforming process," International Journal of Materials and Product Technology, vol. 63, no. 1–2, pp. 109–122. DOI:10.1504/IJMPT.2021.117032

[30] V. Modanloo, V. Alimirzaloo, and M. Elyasi, 2020, "Optimal Design of Stamping Process for Fabrication of Titanium Bipolar Plates Using the Integration of Finite Element and Response Surface Methods," Arab J Sci Eng, vol. 45, no. 2, pp. 1097–1107. DOI:10.1007/s13369-019-04232-8

[31] F. Dundar, E. Dur, S. Mahabunphachai, and M. Koç, 2010, "Corrosion resistance characteristics of stamped and hydroformed proton exchange membrane fuel cell metallic bipolar plates," J Power Sources, vol. 195, no. 11, pp. 3546–3552. DOI:10.1016/j.jpowsour.2009.12.040

[32] D. Qiu, P. Yi, L. Peng, and X. Lai, 2013 "Study on shape error effect of metallic bipolar plate on the GDL contact pressure distribution in proton exchange membrane fuel cell," Int J Hydrogen Energy, vol. 38, no. 16, pp. 6762–6772. DOI:10.1016/j.ijhydene.2013.03.105

[33] H. Talebi-Ghadikolaee, M. Elyasi, S. Seddighi, F. A. Khatir, and V. Modanloo, 2024, "Characterization and prediction of micro channel depth of ultra-thin bipolar plates for PEMFCs," Journal of Engineering Research (Kuwait). DOI:10.1016/j.jer.2024.01.027

[34] S. Shimpalee, V. Lilavivat, J. W. Van Zee, H. McCrabb, and A. Lozano-Morales, 2011, "Understanding the effect of channel tolerances on performance of PEMFCs," Int J Hydrogen Energy, vol. 36, no. 19, pp. 12512–12523. DOI:10.1016/j.ijhydene.2011.06.146

[35] L. Krüger, T. Zeckey, S. Wegt, and S. Jakirlic, 2023, "Flow guidance in the cooling system of a fuel cell: a computational study," in Proceedings of the International Symposium on Turbulence, Heat and Mass Transfer. DOI:10.1615/ICHMT.THMT-23.1110

[36] S.Dinesh, A.Godwin Antony, S.Karuppusamy, V.Vijayan and B.Suresh Kumar, 2016. Experimental investigation and optimization of machining parameters in CNC turning operation of duplex stainless steel. Asian Journal of Research in Social Sciences and Humanities 6,pp. 179-195. DOI:10.5958/2249-7315.2016.01006.6

[37] S.Dinesh, A.Godwin Antony, K.Rajaguru and V.Vijayan. 2016. Experimental investigation and optimization of material removal rate and surface roughness in CNC turning of EN24 alloy steel, Mechanics and Mechanical Engineering, 20 (4) 451—466. DOI:10.5958/2249-7315.2016.00654.7

[38] T.Tamizharasan, N.Senthil Kumar, V.Selvkumar, S.Dinesh, 2019. Taguchi's Methodology of optimizing turning parameters over chip thickness ratio in machining PM AMMC, SN Appl. Sci. 1: 160., Springer Publishers. DOI:10.1007/s42452-019-0170-8